PAPER

Check for updates

Design guidelines for a high-performance hard carbon anode in sodium ion batteries†

Jong Chan Hyun,‡[a] Hyeong Min Jin, [ID] ‡[bc] Jin Hwan Kwak,[d] Son Ha,[a] Dong Hyuk Kang,[a] Hyun Soo Kim,[a] Sion Kim,[a] Minhyuck Park,[a] Chan Yeol Kim,[a] Juhee Yoon,[e] Ji Sung Park,[bc] Ji-Young Kim,[f] Hee-Dae Lim, [ID] [g] Se Youn Cho,[h] Hyoung-Joon Jin[e] and Young Soo Yun [ID] *[adi]

Unclear information on materials design significantly hinders the construction of enhanced hard carbon anodes with high sodium plateau capacities (SPCs). The pore volume ratio of hard carbon imposes thermodynamic limitations on the theoretical sodium plateau capacities (T-SPCs); however, relying solely on its pore structures is not sufficient to predict the practicable SPCs. This study entailed an investigation of a key kinetic parameter of hard carbons that mainly affects the coefficient of capacity utilization (CCU) of SPCs by using a series of polymeric hard carbons (PHCs) with different microstructures. A systematic study revealed a close relationship between the 2D to G band intensity ratio (I_{2D}/I_G) in the Raman spectrum and the internal kinetic barrier for sodium-ion transfer. On the basis of the thermodynamic and kinetic parameters, the structural indicator referred to as the SPC factor was devised to characterize the CCU for SPCs. The SPC factor clearly describes an optimal hard carbon anode as one that possesses a high closed pore volume ratio and low I_{2D}/I_G value. The highest SPC of ~400 mA h g^{-1} was achieved through simple microstructural tuning of the PHCs, demonstrating the feasibility of the proposed design guidelines for a high-performance hard carbon anode for sodium-ion batteries.

Broader context

Sodium ion batteries (SIBs) have garnered significant attention as a viable alternative to lithium-ion batteries (LIBs), owing to the availability of abundant sodium resources and chemistries compatible with well-established LIB technologies. However, poor sodium-ion storage capacities of graphite-like materials, which have driven the commercialization of LIBs, make their application increasingly challenging. This report for the first time introduces design guidelines for a high-performance hard carbon anode for SIBs. On the basis of these guidelines, a significantly high reversible sodium plateau capacity of ~400 mA h g^{-1} was achieved, which is the highest value previously reported for hard carbon anodes.

Introduction

Sodium-ion batteries (SIBs) represent a next-generation power source based on earth-abundant sodium resources and feasible chemistries compatible with well-established lithium-ion battery (LIB) technologies.[1–3] The SIBs have considerable potential in the core application fields of the Industry 4.0 such as electric vehicles, urban air mobility, humanoid robots, and large-scale

[a] KU-KIST Graduate School of Converging Science and Technology, Korea University, Seoul 02841, South Korea. E-mail: c-ysyun@korea.ac.kr

[b] Department of Organic Materials Engineering, Chungnam National University, Daejeon 34134, Republic of Korea

[c] Department of Materials Science and Engineering, Chungnam National University, 99 Daehak-ro, Yuseong-gu, Daejeon 34134, Republic of Korea

[d] Energy Storage Research Center, Korea Institute of Science and Technology (KIST), 5, 14-gil, Hwaraong-ro, Seoul 02792, South Korea

[e] Department of Polymer Science and Engineering, Inha University, Incheon 22212, South Korea

[f] Advanced Analysis & Data Center, Korea Institute of Science and Technology, 5, Hwarang-ro 14-gil, Seongbuk-gu, Seoul 02792, South Korea

[g] Department of Chemical Engineering, Hanyang University, Seoul 04763, South Korea

[h] Carbon Composite Materials Research Center, Institute of Advanced Composite Materials, Korea Institute of Science and Technology (KIST), 92 chudong-ro, Bongdong-eup, Wanju, Jeollabukdo 55324, South Korea

[i] Department of Integrative Energy Engineering, Korea University, 145 Anam-ro, Seongbuk-gu, Seoul 02841, South Korea

† Electronic supplementary information (ESI) available. See DOI: https://doi.org/10.1039/d4ee00315b

‡ Authors contributed equally.

2856 | *Energy Environ. Sci.*, 2024, **17**, 2856–2863

This journal is © The Royal Society of Chemistry 2024

energy storage devices. However, their inferior energy density has been a significant barrier to penetrating the predominant LIB markets.[3–5] In addition, poor sodium-ion storage capacities of graphite-like materials, which have driven the commercialization of LIBs, make their application increasingly challenging.[6–8] Therefore, potential candidates for a feasible anode material have been extensively explored in the last decade.[9–12] Nevertheless, a competitive active anode material for SIBs to comprehensively correspond to the electrochemical performances of lithium–graphite intercalation compounds (Li$^+$–GIC) in LIB systems remains to be realized.

Disordered graphitic carbons, called hard carbons, have long been considered a potential anode candidate for SIBs because of their inexpensive and simple fabrication process and well-balanced electrochemical characteristics.[6–8] The sodium-ion storage profiles of hard carbons under galvanostatic conditions reveal a long-range sodium plateau capacity (SPC) at 0.1 V vs. Na$^+$/Na similar to that of the Li$^+$–GICs.[13–21] Despite their similarity, the low-voltage sodium-ion storage mechanism has been revealed as a nanopore-filling mechanism through a pseudo-metallic nanoclustering reaction, which is remarkably distinct from the lithium intercalation reaction mechanism of the Li$^+$–GICs.[19–21] Accordingly, the nanoscale closed pore is considered a key factor impacting the SPCs of hard carbon anodes.[21–25] The close relationship between the closed pore volume ratio and SPC has been demonstrated for several different types of hard carbons.[18–25] However, owing to the intricate and entangled microstructures of hard carbons composed of multitudinous disordered graphitic lattices, a considerable amount of closed pores remains unavailable even in the fully sodiated state. This results in an insufficient and broad range of SPCs of approximately 100–250 mA h g^{-1}.[23–34] Furthermore, comprehension regarding a central parameter to determine feasible SPCs is lacking. Consequently, information on materials design to construct enhanced hard carbon anodes in SIBs is scarce.

This study systematically investigated a series of polymeric hard carbons (PHCs) to identify a key structural parameter closely related to the SPCs of hard carbon anodes. Several typical microstructural factors of the PHC series, such as the d-spacing, planar (L_a) and out-of-plane (L_c) domain sizes of graphitic carbon crystallites, pore diameter, pore volume ratio, and particle density, cannot explain their SPC variation trend, particularly for hard carbons with large gaps between the SPC and theoretical SPC (T-SPC). In contrast, the proposed structural indicator, referred to as the SPC factor, based on the pore volume ratio and 2D to G band intensity ratio (I_{2D}/I_G) in the Raman spectrum, shows a linear relationship with the coefficient of capacity utilization (CCU, SPC/T-SPC). The introduction of the SPC factor provides specific guidelines for the materials design to realize high-performance PHC anodes in SIBs. On the basis of these guidelines, a high-performance hard carbon anode with the highest reversible SPC of ∼400 mA h g^{-1} was obtained through a controlled chemical activation process. This result demonstrates the significant potential of PHCs in SIBs, surpassing the theoretical lithium plateau capacity of Li$^+$–GICs in LIB systems.

Results and discussion

For the transmutation of the macromolecular structure of waste polyethylene terephthalate (PET) precursors, thermal oxidation was performed at different temperatures – 280, 320, 350, and 380 °C – for 30 min (Supplementary Text 1, Fig. S1–S6 and Table S1, ESI†).[35–37] Thereafter, the PET precursors with the precisely manipulated molecular structures were subjected to high-temperature heating at 1200, 1600, 2000, 2400, and 2800 °C, resulting in the PHC-series samples having different microstructures. The fabricated PHC-series samples were named according to their oxidation–heating temperatures (e.g., O280 – 1200, O280–1600, ..., and O380 – 2800). The crystallographic microstructures of the PHC series were characterized using X-ray diffraction (XRD), Raman spectroscopy, and high-resolution transmission electron microscopy (HR-TEM) (Supplementary Text 2, Fig. S7–S12 and Table S2, ESI†).[38] In addition, the pore structures of the PHC series were characterized via model fitting of the small-angle X-ray scattering (SAXS) data (Supplementary Text 3–4, Fig. S13–S15 and Table S3, ESI†).[39–41]

As shown in Fig. 1(a), (b) and Table S2 (ESI†), the L_a and L_c values of the PHC series gradually increased from 1.82 to 53.01 nm and from 0.97 to 33.67 nm, respectively, upon increasing the heating temperature from 1200 to 2800 °C. The oxidation temperature also affected the L_a and L_c values. Apart from minor exceptions, the L_a and L_c values of the PHC series gradually increased from 1.82–4.68 and 0.97–12.06 nm to 2.07–53.01 and 1.07–33.67 nm, respectively, upon increasing the oxidation temperatures from 280 to 380 °C. In contrast, the d-spacing values of the graphitic lattices in the PHC series gradually decreased from 3.99 to 3.37 Å with increasing heating temperature from 1200 to 2800 °C (Fig. 1c and Table S2, ESI†).[38] These results indicate that the graphitic structures continuously develop into denser structures with increasing heating temperature, and higher oxidation temperatures contribute to greater densification. With the development of the ordered graphitic domains, the average pore diameter of the PHC series also gradually increased from 3.75 to 55.63 Å, depending on the heating temperatures (Fig. 1d). In contrast to the continuous shifts of L_a, L_c, d-spacing, and pore diameter in one direction toward higher values, the particle densities of the PHC series changed in an inverse parabolic curve shape (Fig. 1e). The reduction in particle density indicated that more closed pores were generated in the internal structure of the PHCs with increasing heating temperature. The variation plots of the closed pore volume ratios, which were calculated from the particle densities by using a previously reported method, are shown in Fig. 1f.[21] The pore volume ratios varied from 11% to 36%; the relatively high-temperature-heated PHC samples (≥2400 °C) generally exhibited higher closed pore volume ratios of ≥30.0%.

To elucidate the pore volume ratio–SPC relationship, the electrochemical sodium-ion storage behaviors of the PHCs were characterized in a half-cell through galvanostatic process at 25 and 60 °C under a current density of 25 mA g^{-1} over a voltage window of 0–2.0 V vs. Na$^+$/Na. The characterized galvanostatic
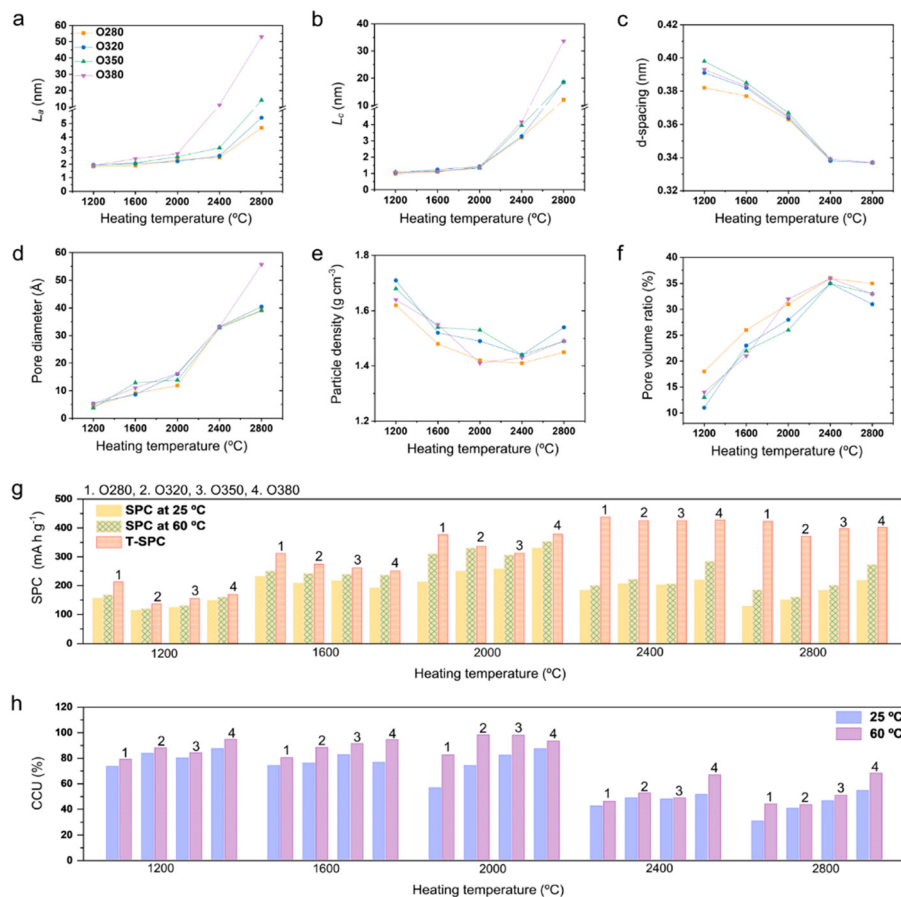
This journal is © The Royal Society of Chemistry 2024

Energy Environ. Sci., 2024, **17**, 2856–2863 | **2857**

Fig. 1 Materials properties of the PHC series and their interconnection with SPCs and CCU values. (a) L_a, (b) L_c, (c) d-spacing, (d) average pore diameter, (e) particle density, and (f) pore volume ratio of the pre-treatment oxidation temperature-based PHC series, and their (g) SPC and (h) CCU bar graphs characterized at different operating temperatures of 25 and 60 °C.

voltage profiles show the signature curve shape of hard carbon corresponding to sloping voltage capacity followed by a long-range SPC (Fig. S16 and S17, ESI†). The SPCs are depicted as bar graphs with the T-SPCs calculated based on the particle densities by using a previously reported method (Fig. 1g).[21] In the relatively low temperature-heated PHC samples of ≤2000 °C, the capacity gap between SPC and T-SPC is relatively smaller, indicating high CCU values of 56.53–87.25% and 78.81–98.16% at the 25 and 60 °C cell tests, respectively (Fig. 1g and h and Table S4, ESI†). These results indicate that most of the closed pore volumes are available in the relatively low temperature-heated samples (≤2000 °C). In contrast, the higher temperature-heated PHCs of ≥2400 °C exhibit much lower CCU values of 30.43–54.23% and 43.10–67.96% at both 25 and 60 °C, respectively. Accordingly, they showed lower SPC capacities than those of the low-temperature-heated samples despite their higher closed pore volume ratios. To examine the origin of this discordance, the interrelation between several structural parameters and SPCs is depicted in Fig. S18 (ESI†). However, none of the conventional structural parameters of hard carbon have a direct relationship with the SPC variation trend.

In contrast, note the 2D to G band intensity ratio (I_{2D}/I_G) in the Raman spectra normalized as the G band (Fig. 2a–d).

The G band ($\sim$1580 cm^{-1}) was induced by the primary Raman-active mode for highly ordered polyhexagonal domains, whereas the 2D band ($\sim$2690 cm^{-1}) originates from second-order Raman scattering by in-plane transverse phonons near the boundary of the Brillouin zone.[42–44] The 2D band is highly sensitive to the local ordering of the graphitic structure and the number of graphene layers. Therefore, the I_{2D}/I_G value can indicate the degree of densified graphitic structures, which can hinder sodium-ion transfer inside hard carbon. Electrochemical impedance spectroscopy (EIS) profiles exhibit the close relationship between I_{2D}/I_G values and charge-transfer resistance (R_{ct}) values (Fig. 2e–h and Fig. S19, ESI†). With increasing I_{2D}/I_G values, the R_{ct} values systematically increased in all series of samples. An increase in the R_{ct} value denotes an augmented resistance to sodium-ion storage mechanisms. With the further development of the graphitic structure, it imposes increased resistance to the penetration of sodium ions into the depths of the hard carbon, culminating in a diminution of the low-voltage plateau capacity. Hence, the lower-temperature-heated PHCs with lower I_{2D}/I_G values were slightly kinetically interrupted during the sodiation process, showing higher CCU values. In contrast, the densely packed graphitic structures of the higher-temperature-heated PHC samples
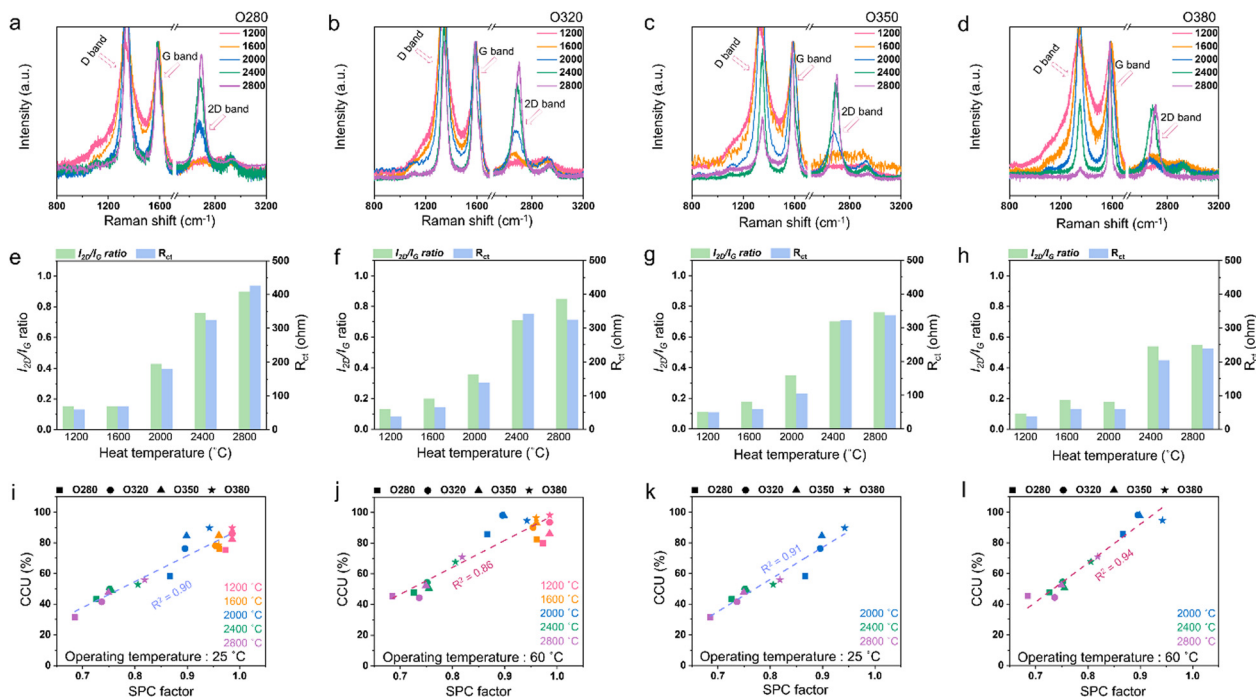
2858 | *Energy Environ. Sci.*, 2024, **17**, 2856–2863

This journal is © The Royal Society of Chemistry 2024

Fig. 2 Introduction of the SPC factor composed of the I_{2D}/I_G ratio in Raman spectrum and pore volume ratio as a key parameter to determine the CCU value. Raman spectra of (a) O280, (b) O320, (c) O350, and (d) O380 series samples. Comparison for the I_{2D}/I_G ratio and R_{ct} value of (e) O280, (f) O320, (g) O350, and (h) O380 series samples. The SPC factor *vs.* CCU value plots of all the PHC series at different operating temperatures of (i) 25 and (j) 60 °C and those of the high-temperature ($\geq$2000 °C)-heated PHC series at different operating temperatures of (k) 25 and (l) 60 °C.

impeded the full utilization of their theoretical pore-filling capacities, leading to extremely low CCU and poor SPC values. On the basis of the experimental results, a simple equation was designed to better understand the interrelation between the CCU, pore volume ratio, and I_{2D}/I_G value, as shown in eqn (1) and (2).

$$\frac{\text{SPC}}{\text{T-SPC}}(\text{CCU}) = a\left(1 - \text{pore volume ratio} \times \frac{I_{2D}}{I_G}\right) + b \quad (1)$$

$$\text{SPC factor} = \left(1 - \text{pore volume ratio} \times \frac{I_{2D}}{I_G}\right) \quad (2)$$

where a and b are the coefficients of SPC and CCU, respectively. a and b can be affected by the operating temperature, precursor material, fabrication process, and other factors. The SPC factor is composed of the pore volume ratio and I_{2D}/I_G value, which indicates a feasible pore volume ratio of hard carbon under a given kinetic condition (Table S4, ESI†). Therefore, the SPC factor is a key structural indicator of the CCU values. The SPC factor *versus* CCU plots of the PHC-series samples show a linear relationship (Fig. 2i–l). The plots reveal the higher coefficient of determination (R^2) values of 0.90 and 0.86 for the half-cell tests at 25 and 60 °C, respectively, in all the series samples (Fig. 2i and j). In the higher temperature-treated PHCs ($\geq$2000 °C), the R^2 values further increased by 0.91 and 0.94 for the half-cell tests at 25 and 60 °C, respectively (Fig. 2k and l). In addition, a similar linear relationship was demonstrated for different types of hard carbon samples prepared using different precursor materials (Fig. S20, ESI†). These results suggest the need to

design a high-performance hard carbon anode for SIBs by increasing the pore volume ratio and lowering the I_{2D}/I_G value.

To demonstrate the validity of the microstructural guidelines for hard carbon anodes, controlled chemical activation using potassium hydroxide was conducted to increase the closed pore volume ratio and simultaneously decrease the local graphitic ordering. The effects of chemical activation on the closed pore volume ratios and graphitic microstructures are discussed in the Supplementary Text 5, ESI.†[45,46] The microstructural tuning with chemical activation was experimentally confirmed using the O280–2400 sample as a platform material, which had the highest pore volume and lowest CCU ($<$0.50) among all the tested samples. Controlled chemical activation was conducted with KOH to O280–2400 weight ratios of 10, 30, and 50 wt%. The activated O280–2400 samples are denoted as A10, A30, and A50. The material properties of A10, A30, and A50 are summarized in the Supplementary Text 6, Fig. S21–S28, Tables S5 and S6 (ESI†).

The galvanostatic discharge/charge profiles of O280–2400, A10, A30, and A50 revealed that the SPCs of the PHCs can be tuned using a controlled activation process (Fig. 3a). The reversible SPC (200 mA h g^{-1}) of the O280–2400 was increased by approximately 330, 400, and 290 mA h g^{-1} for A10, A30, and A50, respectively (Fig. 3b). The improvement in the SPCs was due to an increase in the SPC factors. The I_{2D}/I_G value (0.73) of the O280–2400 gradually decreased to 0.48, 0.45, and 0.54, whereas the pore volume ratio (36%) gradually increased to 38%, 41%, and 43% for A10, A30, and A50, respectively (Fig. 3c and Table S7, ESI†). Accordingly, the SPC factor (0.73) of
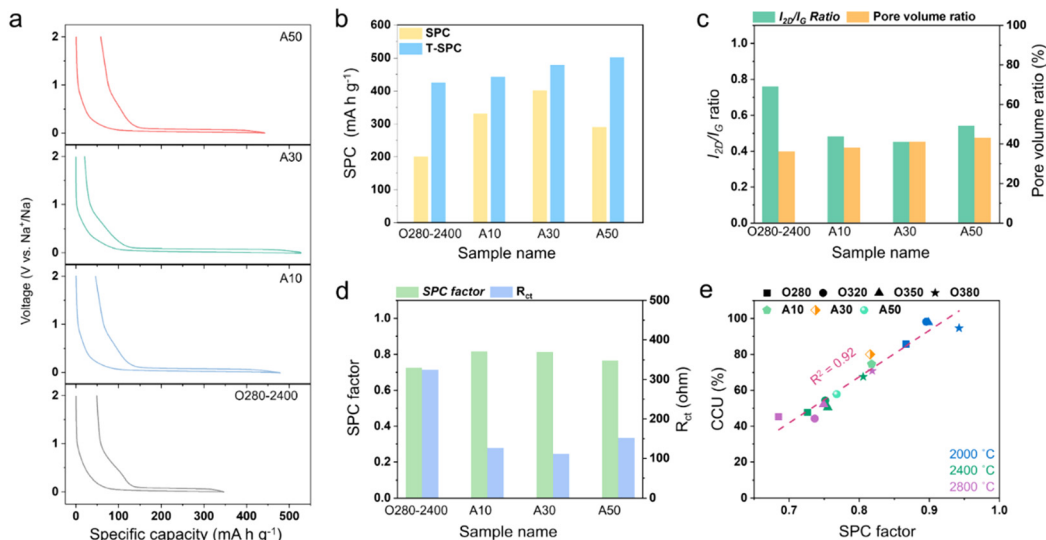
Fig. 3 Demonstration of the close relationship between SPC factor and CCU in the microstructure-tuned PHC samples; O280–2400, A10, A30, and A50, obtained at an operating temperature of 60 °C. (a) Galvanostatic discharge/charge profiles. Comparison bar graphs for (b) SPC and T-SPC, (c) I_{2D}/I_G value and pore volume ratio, and (d) SPC factor and R_{ct}. (e) SPC factor *vs.* CCU value plots.

the O280–2400 increased by 0.82, 0.82, and 0.77, and its R_{ct} value (325 Ω) significantly reduced by 126, 111, and 152 Ω for A10, A30, and A50, respectively (Fig. 3d and Fig. S28 and Table S7, ESI†). In addition, the T-SPC of the activated PHCs gradually increased from 443 to 501 mA h g^{-1} owing to their increasing pore volume ratios, resulting in a large increase in the SPCs (Fig. 3b and c). The SPC factor *vs.* CCU plots of the microstructure-tuned PHC samples reveal a linear relationship with high R^2 values of 0.92 (Fig. 3e). These results evidently indicate the effectiveness of the SPC–CCU relationship equation based on the structural parameter I_{2D}/I_G (eqn (1)).

To elucidate that the increased SPCs originated from the pore-filling mechanism, and not the sodium intercalation behavior between the expanded graphitic lattices that were chemically activated, *in situ* XRD and Raman spectral characterization studies were conducted for the high-performance A30 sample (Fig. 4a and b). In the *in situ* XRD patterns for 1st cycle, the graphite (002) peak was observed at 25.9°, which did not change during the overall discharge/charge process, indicating that a slight sodium intercalation reaction occurred (Fig. 4a). In addition, the *in situ* Raman spectra showed no distinctive changes in the signature D, G, and 2D bands during the discharge/charge cycle, indicating that the sodiation process did not accompany structural transition, even in the local areas (Fig. 4b). These results agree with the previously reported pore-filling mechanism for hard carbon anodes.[18–25] Furthermore, a galvanostatic sequential sodiation–lithiation test was conducted *via* full sodiation in sodium half-cells, followed by full lithiation of the fully sodiated samples in lithium half-cells (Fig. 4c and d). In the fully sodiated states after sodiation by ∼0.32 V *vs.* Li$^+$/Li, additional lithium intercalation reactions occurred in both the O280–2400 and A30 samples, and most of the lithiation capacities were reversibly extracted during delithiation. The reversible lithium intercalation capacities

are similar to their original lithium intercalation capacities although the additional lithiation was conducted only in a narrow voltage window of approximately 0.32 V (Fig. S29, ESI†). In addition, the reversible lithiation behaviors were well-maintained during 10 cycles (Fig. S30, ESI†). Following the desodiation process, the remaining sodium was reversibly extracted from the O280–2400 and A30. These results prove that the graphitic lattices were nearly empty, even after full sodiation; therefore, the increased SPC was due to the increased pore-filling capacity. In addition, the sodiation process is accompanied by relatively low volume expansion of <4% compared with that (∼7%) of the sequential lithiation process, despite its higher SPC (Fig. 4e). The lower volume expansion is evidence for the poor two-phase sodium intercalation reaction, and at the same time, it reveals a high potential of the hard carbon anode for SIBs.

Additionally, the comparative advantage of hard carbon anodes and the importance of their microstructural design for application in SIBs are displayed in the comparison plots. These plots show the specific capacities and average voltages of previously reported carbon-based anode materials (Fig. 4f). Several nanocarbons based on surface and/or bulk chemisorption mechanisms show reversible capacities of 120–380 mA h g^{-1} and high voltage of 1.0–1.6 V.[53–71] In the case of hard carbons, higher reversible capacities of 220–480 mA h g^{-1} and lower average voltage ranges of 0.2–0.6 V were achieved.[15–17,19,20,22–34,47–52] The PHC-series samples in this study also showed reversible capacities and voltages similar to those of previously reported hard carbon materials. However, the microstructure-tuned A30 exhibited the highest SPC and overall capacity of ∼400 and ∼507 mA h g^{-1}, respectively, among all the reported hard carbons, including the PHC series. In addition, the A30 showed great rate-cycling performance and reversibility (Fig. S31, ESI†). The reversibility of the nanopore-filling sodiation behaviors was proved by *ex situ* analysis
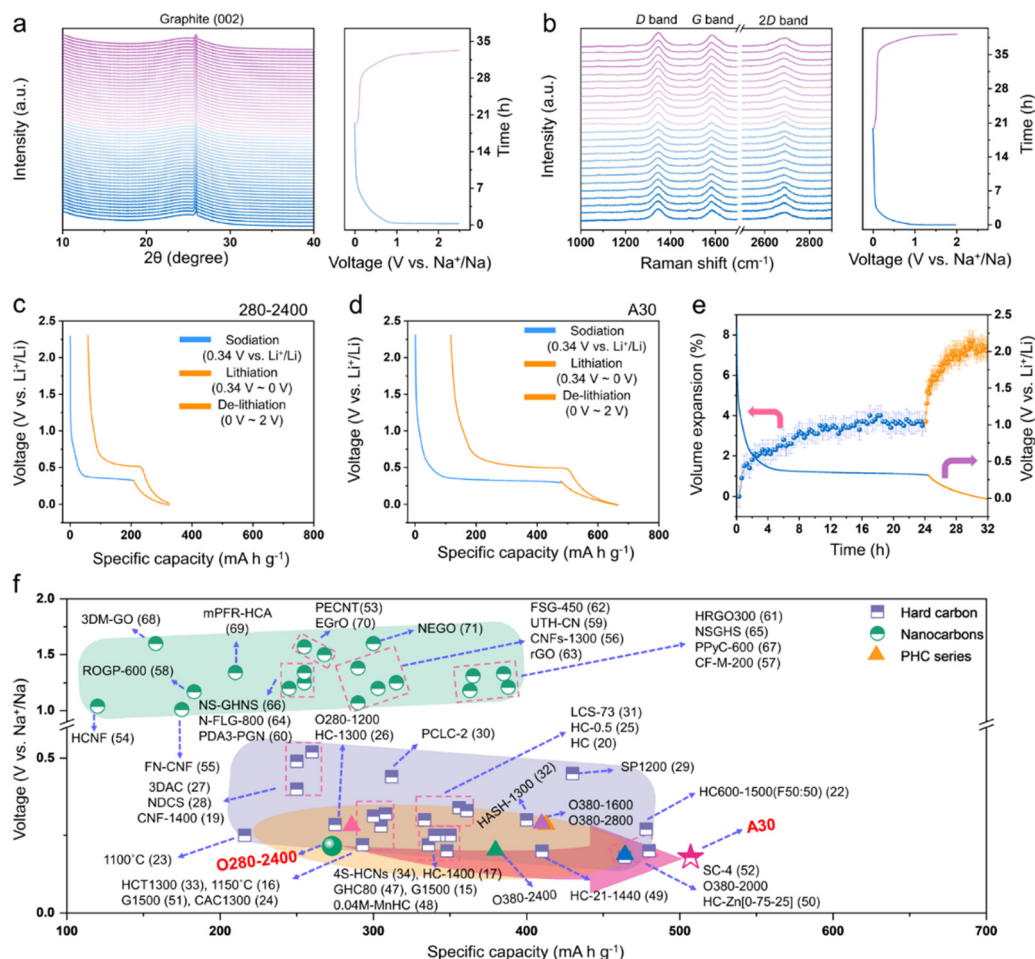
2860 | *Energy Environ. Sci.*, 2024, **17**, 2856–2863

This journal is © The Royal Society of Chemistry 2024

Fig. 4 Confirmation results of a pore-filling sodiation mechanism on A30, and comparing data of SPCs. (a) *In situ* XRD patterns and (b) *in situ* Raman spectra of A30 characterized during the initial discharge/charge cycle. Sequential sodiation–lithiation/extraction profiles of (c) 280–2400 and (d) A30, and (e) operando volume expansion data characterized during the sodiation and lithiation process. (f) Comparison plots of reversible capacity with those of the previously reported carbon-based anode materials.

(Supplementary Text 7 and Fig. S32, ESI†). Considering the T-SPCs and their CCU values of the different PHC samples, further improved reversible capacities and comprehensively well-balanced electrochemical performances can be achieved by more meticulous materials design according to the guidelines based on the structural indicator SPC factor.

controlled chemical activation method to increase the closed pore volume ratio and concurrently lower the I_{2D}/I_G value. The microstructure-tuned PHC exhibited a significantly high reversible SPC of $\sim$400 mA h g^{-1} and an overall reversible capacity of 507 mA h g^{-1}, which is the highest value previously reported for hard carbon anodes.

Conclusions

In summary, the close relationship between 2D the G band intensity ratio (I_{2D}/I_G) in the Raman spectrum and the internal kinetic barrier for sodium-ion transfer was elucidated. In addition, a structural indicator, SPC factor, composed of the I_{2D}/I_G value and the closed pore volume ratio, was developed to predict the CCU values of the SPCs. The linear relationship between the SPC factor and CCU was demonstrated using multiple series of PHCs with different graphitic microstructures and closed pore volume ratios. According to the design guidelines based on the SPC factor, the microstructures of the PHC, which have a poor CCU value, were tuned using a

Author contributions

This journal is © The Royal Society of Chemistry 2024

Energy Environ. Sci., 2024, **17**, 2856–2863 | **2861**

Conflicts of interest

There are no conflicts to declare.

Acknowledgements

Notes and references

1 Y. Li, A. Vasileiadis, Q. Zhou, Y. Lu, Q. Meng, Y. Li, P. Ombrini, J. Zhao, Z. Chen, Y. Niu, X. Qi, F. Xie, R. Van Der Jagt, S. Ganapathy, M.-M. Titirici, H. Li, L. Chen, M. Wagemaker and Y.-S. Hu, *Nat. Energy*, 2024, **9**, 134–142.

2 R. Usiskin, Y. Lu, J. Popovic, M. Law, P. Balaya, Y.-S. Hu and J. Maier, *Nat. Rev. Mater.*, 2021, **6**, 1020–1035.

3 Z. Tang, R. Zhang, H. Wang, S. Zhou, Z. Pan, Y. Huang, D. Sun, Y. Tang, X. Ji, K. Amine and M. Shao, *Nat. Commun.*, 2023, **14**, 6024.

4 A. Rudola, R. Sayers, C. J. Wright and J. Barker, *Nat. Energy*, 2023, **8**, 215–218.

5 Y.-J. Guo, P.-F. Wang, Y.-B. Niu, X.-D. Zhang, Q. Li, X. Yu, M. Fan, W.-P. Chen, Y. Yu, X. Liu, Q. Meng, S. Xin, Y.-X. Yin and Y.-G. Guo, *Nat. Commun.*, 2021, **12**, 5267.

6 Y. S. Yun, K. Park, B. Lee, S. Y. Cho, Y. Park, S. J. Hong, B. H. Kim, H. Gwon, H. Kim, S. Lee, Y. W. Park, H. Jin and K. Kang, *Adv. Mater.*, 2015, **27**, 6914–6921.

7 Y. Zheng, Y. Wang, Y. Lu, Y.-S. Hu and J. Li, *Nano Energy*, 2017, **39**, 489–498.

8 C. M. Ghimbeu, B. Zhang, A. M. Yuso, B. Réty and J.-M. Tarascon, *Carbon*, 2019, **153**, 634–647.

9 C. Zheng, D. Ji, Q. Yao, Z. Bai, Y. Zhu, C. Nie, D. Liu, N. Wang, J. Yang and S. Dou, *Angew. Chem., Int. Ed.*, 2023, **62**, e202214258.

10 M. G. Boebinger, D. Yeh, M. Xu, B. C. Miles, B. Wang, M. Papakyriakou, J. A. Lewis, N. P. Kondekar, F. J. Q. Cortes, S. Hwang, X. Sang, D. Su, R. R. Unocic, S. Xia, T. Zhu and M. T. Mcdowell, *Joule*, 2018, **2**, 1783–1799.

11 X. Xu, C. Niu, M. Duan, X. Wang, L. Huang, J. Wang, L. Pu, W. Ren, C. Shi, J. Meng, B. Song and L. Mai, *Nat. Commun.*, 2017, **8**, 460.

12 T. Deng, X. Ji, L. Zou, O. Chiekezi, L. Cao, X. Fan, T. R. Adebisi, H.-J. Chang, H. Wang, B. Li, X. Li, C. Wang, D. Reed, J.-G. Zhang, V. L. Sprenkle, C. Wang and X. Lu, *Nat. Nanotechnol.*, 2022, **17**, 269–277.

13 X. Dou, I. Hasa, D. Saurel, C. Vaalma, L. Wu, D. Buchholz, D. Bresser, S. Komaba and S. Passerini, *Mater. Today*, 2019, **23**, 87–104.

14 M. E. Lee, S. M. Lee, J. Choi, D. Jang, S. Lee, H. Jin and Y. S. Yun, *Small*, 2020, **16**, 2001053.

15 Z. Guo, Z. Xu, F. Xie, J. Jiang, K. Zheng, S. Alabidun, M. Crespo-Ribadeneyra, Y. Hu, H. Au and M. Titirici, *Adv. Mater.*, 2023, **35**, 2304091.

16 D. A. Stevens and J. R. Dahn, *J. Electrochem. Soc.*, 2000, **147**, 1271.

17 Y. Morikawa, S. Nishimura, R. Hashimoto, M. Ohnuma and A. Yamada, *Adv. Energy Mater.*, 2020, **10**, 1903176.

18 J. M. Stratford, P. K. Allan, O. Pecher, P. A. Chater and C. P. Grey, *Chem. Commun.*, 2016, **52**, 12430–12433.

19 B. Zhang, C. M. Ghimbeu, C. Laberty, C. Vix-Guterl and J. Tarascon, *Adv. Energy Mater.*, 2016, **6**, 1501588.

20 Z. Wang, X. Feng, Y. Bai, H. Yang, R. Dong, X. Wang, H. Xu, Q. Wang, H. Li, H. Gao and C. Wu, *Adv. Energy Mater.*, 2021, **11**, 2003854.

21 H. Kim, J. C. Hyun, D. Kim, J. H. Kwak, J. B. Lee, J. H. Moon, J. Choi, H. Lim, S. J. Yang, H. M. Jin, D. J. Ahn, K. Kang, H. Jin, H. Lim and Y. S. Yun, *Adv. Mater.*, 2023, **35**, 2209128.

22 A. Kamiyama, K. Kubota, D. Igarashi, Y. Youn, Y. Tateyama, H. Ando, K. Gotoh and S. Komaba, *Angew. Chem., Int. Ed.*, 2021, **60**, 5114–5120.

23 J. M. Stratford, A. K. Kleppe, D. S. Keeble, P. A. Chater, S. S. Meysami, C. J. Wright, J. Barker, M.-M. Titirici, P. K. Allan and C. P. Grey, *J. Am. Chem. Soc.*, 2021, **143**, 14274–14286.

24 K. Wang, F. Sun, H. Wang, D. Wu, Y. Chao, J. Gao and G. Zhao, *Adv. Funct. Mater.*, 2022, **32**, 2203725.

25 L. Xiao, H. Lu, Y. Fang, M. L. Sushko, Y. Cao, X. Ai, H. Yang and J. Liu, *Adv. Energy Mater.*, 2018, **8**, 1703238.

26 S. Alvin, H. S. Cahyadi, J. Hwang, W. Chang, S. K. Kwak and J. Kim, *Adv. Energy Mater.*, 2020, **10**, 2000283.

27 P. Lu, Y. Sun, H. Xiang, X. Liang and Y. Yu, *Adv. Energy Mater.*, 2018, **8**, 1702434.

28 T. Yang, T. Qian, M. Wang, X. Shen, N. Xu, Z. Sun and C. Yan, *Adv. Mater.*, 2016, **28**, 539–545.

29 N. Sun, H. Liu and B. Xu, *J. Mater. Chem. A*, 2015, **3**, 20560–20566.

30 H. Chen, N. Sun, Y. Wang, R. A. Soomro and B. Xu, *Energy Storage Mater.*, 2023, **56**, 532–541.

31 H. Chen, N. Sun, Q. Zhu, R. A. Soomro and B. Xu, *Adv. Sci.*, 2022, **9**, 2200023.

32 Y. Zhu, M. Chen, Q. Li, C. Yuan and C. Wang, *Carbon*, 2018, **129**, 695–701.

33 Y. Li, Y. Hu, M. Titirici, L. Chen and X. Huang, *Adv. Energy Mater.*, 2016, **6**, 1600659.

34 D. Bin, Y. Li, Y. Sun, S. Duan, Y. Lu, J. Ma, A. Cao, Y. Hu and L. Wan, *Adv. Energy Mater.*, 2018, **8**, 1800855.

35 M. Enayati, S. Mohammadi and M. G. Bouldo, *ACS Sustainable Chem. Eng.*, 2023, **11**, 16618–16626.

36 Y. Hu, Z. Gao, J. Yang, H. Chen and L. Han, *J. Colloid Interface Sci.*, 2019, **538**, 481–488.

37 L. H. Buxbaum, *Angew. Chem., Int. Ed. Engl.*, 1968, **7**, 182–190.

38 S. Y. Cho, Y. S. Yun, D. Jang, J. W. Jeon, B. H. Kim, S. Lee and H.-J. Jin, *Nat. Commun.*, 2017, **8**, 74.

39 D. Saurel, J. Segalini, M. Jauregui, A. Pendashteh, B. Daffos, P. Simon and M. Casas-Cabanas, *Energy Storage Mater.*, 2019, **21**, 162–173.

2862 | *Energy Environ. Sci.*, 2024, **17**, 2856–2863

This journal is © The Royal Society of Chemistry 2024

40 S. H. Song, H. S. Kim, K. S. Kim, S. Hong, H. Jeon, J. Lim, Y. H. Jung, H. Ahn, J. D. Jang, M.-H. Kim, J. H. Seo, J.-H. Kwon, D. Kim, Y. J. Lee, Y.-S. Han, K.-Y. Park, C. Kim, S.-H. Yu, H. Park, H. M. Jin and H. Kim, *Adv. Funct. Mater.*, 2023, **34**, 2306654.

41 J. Ilavsky and P. R. Jemian, *J. Appl. Crystallogr.*, 2009, **42**, 347–353.

42 A. C. Ferrari and D. M. Basko, *Nat. Nanotechnol.*, 2013, **8**, 235–246.

43 A. C. Ferrari, J. C. Meyer, V. Scardaci, C. Casiraghi, M. Lazzeri, F. Mauri, S. Piscanec, D. Jiang, K. S. Novoselov, S. Roth and A. K. Geim, *Phys. Rev. Lett.*, 2006, **97**, 187401.

44 D. B. Schuepfer, F. Badaczewski, J. M. Guerra-Castro, D. M. Hofmann, C. Heiliger, B. Smarsly and P. J. Klar, *Carbon*, 2020, **161**, 359–372.

45 M. A. Lillo-Ródenas, D. Cazorla-Amorós and A. Linares-Solano, *Carbon*, 2003, **41**, 267–275.

46 N. R. Kim, S. M. Lee, M. W. Kim, H. J. Yoon, W. G. Hong, H. J. Kim, H. J. Choi, H.-J. Jin and Y. S. Yun, *Adv. Energy Mater.*, 2017, **7**, 1700629.

47 H. Zhang, W. Zhang and F. Huang, *Chem. Eng. J.*, 2022, **434**, 134503.

48 J. Zhao, X. He, W. Lai, Z. Yang, X. Liu, L. Li, Y. Qiao, Y. Xiao, L. Li, X. Wu and S. Chou, *Adv. Energy Mater.*, 2023, **13**, 2300444.

49 Q. Meng, Y. Lu, F. Ding, Q. Zhang, L. Chen and Y.-S. Hu, *ACS Energy Lett.*, 2019, **4**, 2608–2612.

50 D. Igarashi, Y. Tanaka, K. Kubota, R. Tatara, H. Maejima, T. Hosaka and S. Komaba, *Adv. Energy Mater.*, 2023, **13**, 2302647.

51 H. Au, H. Alptekin, A. C. S. Jensen, E. Olsson, C. A. O'Keefe, T. Smith, M. Crespo-Ribadeneyra, T. F. Headen, C. P. Grey, Q. Cai, A. J. Drew and M.-M. Titirici, *Energy Environ. Sci.*, 2020, **13**, 3469–3479.

52 Q. Li, X. Liu, Y. Tao, J. Huang, J. Zhang, C. Yang, Y. Zhang, S. Zhang, Y. Jia, Q. Lin, Y. Xiang, J. Cheng, W. Lv, F. Kang, Y. Yang and Q.-H. Yang, *Natl. Sci. Rev.*, 2022, **9**, nwac084.

53 A. P. V. K. Saroja, M. Muruganathan, K. Muthusamy, H. Mizuta and R. Sundara, *Nano Lett.*, 2018, **18**, 5688–5696.

54 Y. Zhong, X. Xia, J. Zhan, X. Wang and J. Tu, *J. Mater. Chem. A*, 2016, **4**, 11207–11213.

55 Z. Wang, L. Qie, L. Yuan, W. Zhang, X. Hu and Y. Huang, *Carbon*, 2013, **55**, 328–334.

56 H. Yang, R. Xu and Y. Yu, *Energy Storage Mater.*, 2019, **22**, 105–112.

57 M. Ning, J. Wen, Z. Duan, X. Cao, G. Qiu, M. Zhang, X. Ye, Z. Li and H. Zhang, *Small*, 2023, **19**, 2301975.

58 Y. S. Yun, Y.-U. Park, S.-J. Chang, B. H. Kim, J. Choi, J. Wang, D. Zhang, P. V. Braun, H.-J. Jin and K. Kang, *Carbon*, 2016, **99**, 658–664.

59 Y. S. Yun, S. Y. Cho, H. Kim, H. Jin and K. Kang, *ChemElectroChem*, 2015, **2**, 359–365.

60 Y. Luo, L. Wang, D. Kim, Q. Li, Y. Kang, Y. Liu, J. Yu, H. Wang and H. Lee, *Energy Storage Mater.*, 2021, **39**, 70–80.

61 J. Zhao, Y. Zhang, F. Zhang, H. Liang, F. Ming, H. N. Alshareef and Z. Gao, *Adv. Energy Mater.*, 2019, **9**, 1803215.

62 A. Mahmood, Z. Yuan, X. Sui, M. A. Riaz, Z. Yu, C. Liu, J. Chen, C. Wang, S. Zhao, N. Mahmood, Z. Pei, L. Wei and Y. Chen, *Energy Storage Mater.*, 2021, **41**, 395–403.

63 G. Zheng, Q. Lin, J. Ma, J. Zhang, Y. He, X. Tang, F. Kang, W. Lv and Q. Yang, *InfoMat*, 2021, **3**, 1445–1454.

64 J. Liu, Y. Zhang, L. Zhang, F. Xie, A. Vasileff and S. Qiao, *Adv. Mater.*, 2019, **31**, 1901261.

65 W. Chen, X. Chen, R. Qiao, Z. Jiang, Z.-J. Jiang, S. Papović, K. Raleva and D. Zhou, *Carbon*, 2022, **187**, 230–240.

66 R. Thangavel, A. G. Kannan, R. Ponraj, G. Yoon, V. Aravindan, D.-W. Kim, K. Kang, W.-S. Yoon and Y.-S. Lee, *Energy Storage Mater.*, 2020, **25**, 702–713.

67 Z. Luo, J. Zhou, X. Cao, S. Liu, Y. Cai, L. Wang, A. Pan and S. Liang, *Carbon*, 2017, **122**, 82–91.

68 Y.-S. Zhang, B.-M. Zhang, Y.-X. Hu, J. Li, C. Lu, M.-J. Liu, K. Wang, L.-B. Kong, C.-Z. Zhao, W.-J. Niu, W.-W. Liu, K. Zhao, M.-C. Liu and Y.-L. Chueh, *Energy Storage Mater.*, 2021, **34**, 45–52.

69 Z.-L. Yu, S. Xin, Y. You, L. Yu, Y. Lin, D.-W. Xu, C. Qiao, Z.-H. Huang, N. Yang, S.-H. Yu and J. B. Goodenough, *J. Am. Chem. Soc.*, 2016, **138**, 14915–14922.

70 Y. Zhang, J. Qin, S. E. Lowe, W. Li, Y. Zhu, M. Al-Mamun, M. Batmunkh, D. Qi, S. Zhang and Y. L. Zhong, *Carbon*, 2021, **177**, 71–78.

71 M. Hu, H. Zhou, X. Gan, L. Yang, Z.-H. Huang, D.-W. Wang, F. Kang and R. Lv, *J. Mater. Chem. A*, 2018, **6**, 1582–1589.

This journal is © The Royal Society of Chemistry 2024

Energy Environ. Sci., 2024, **17**, 2856–2863 | **2863**